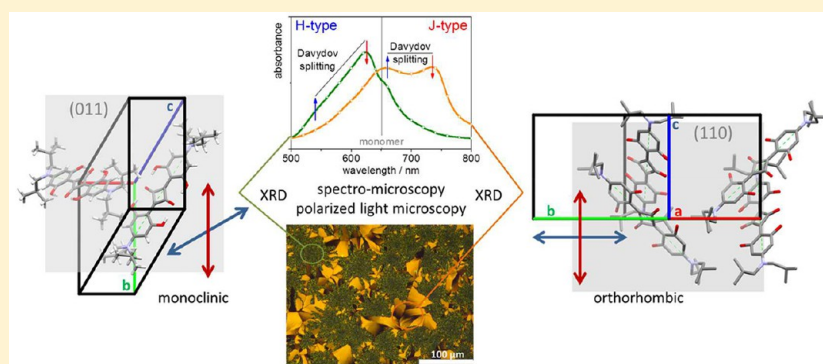


## Spotlight on Excitonic Coupling in Polymorphic and Textured Anilino Squaraine Thin Films

Frank Balzer,<sup>†</sup> Heiko Kollmann,<sup>‡</sup> Matthias Schulz,<sup>#</sup> Gregor Schnakenburg,<sup>§</sup> Arne Lützen,<sup>#</sup> Marc Schmidtman,<sup>||</sup> Christoph Lienau,<sup>‡</sup> Martin Silies,<sup>‡</sup> and Manuela Schiek<sup>\*,†,||</sup><sup>†</sup>Mads Clausen Institute, University of Southern Denmark, Alsion 2, DK-6400 Sønderborg, Denmark<sup>‡</sup>Ultrafast Nanooptics, Institute of Physics, <sup>||</sup>Department of Chemistry, and <sup>†</sup>Energy and Semiconductor Research Laboratory, Institute of Physics, University of Oldenburg, D-26111 Oldenburg, Germany<sup>#</sup>Kekulé Institute of Organic Chemistry and Biochemistry and <sup>§</sup>Institute of Inorganic Chemistry, Rheinische-Friedrich-Wilhelms-University of Bonn, Gerhard-Domagk-Strasse 1, D-53121 Bonn, Germany

## S Supporting Information



**ABSTRACT:** Structural diffraction analysis of an anilino squaraine with *branched* isobutyl side chains shows crystallization into two polymorphic structures in the bulk and in spin-casted thin films. We observe multi-peaked and pleochroic absorption spectra being blue-(red)-shifted for the monoclinic (orthorhombic) polymorph. We understand the packing as Coulombic molecular H-(J)-aggregates supporting Davydov splitting. Pictures of projected Davydov components in oriented thin films fit well to polarization resolved spectro-microscopy and crossed-polarized light microscopy investigations. By comparison with literature on anilino squaraines with *linear* alkyl side chains, we point out a general trend for steering the thin film excitonic properties by simple side chain and/or processing condition variation. Combined with the ability to locally probe the direction of transition dipole moments, this adds value to the rational design of functional thin films for optoelectronic applications, especially envisioning ultrastrong light–matter interactions.

## ■ INTRODUCTION

Squaraines are small molecular quadrupolar donor–acceptor–donor (D–A–D) chromophores, Figure 1, that are readily available through environmentally friendly condensation reactions.<sup>1,2</sup> They are appealing not just because of their intense color and quasimetallic reflection in the crystalline state<sup>3</sup> and polymorphic diversity,<sup>4,5</sup> but also due to their versatility. Owing to their quadrupolar nature,<sup>6,7</sup> squaraines have a large two-photon absorption cross section.<sup>8,9</sup> Thus, they are widely used as near infrared (NIR) fluorescent probes for bioimaging<sup>10,11</sup> and for photodynamic therapy.<sup>12</sup> Squaraines have become famous for their photoconducting properties as xerographic materials,<sup>13</sup> and are well established as photovoltaic materials in modern organic solar cells.<sup>14–23</sup> Especially 2,4-bis[4-(*N,N*-diisobutylamino)-2,6-dihydroxyphenyl]squaraine (SQIB) is a model anilino squaraine with *branched* alkyl side chains suitable for solution processing as well as thermal vapor deposition. It is among the cheapest materials relevant for

photovoltaic applications,<sup>24</sup> and it has been implemented in organic solar cells by several groups.<sup>25–32</sup> Furthermore, it was investigated for its ultrastrong exciton–polariton coupling in a microcavity<sup>33</sup> as well as exciton–plasmon coupling in a silver nanoshell.<sup>34</sup>

In general, the excitonic properties of condensed organic matter are dictated by their molecular packing. For small organic molecules, polymorphism in bulk crystals<sup>35,36</sup> or crystalline thin films supported on surfaces<sup>37–39</sup> is very common. The aggregation and consequently the excitonic properties and resulting optoelectronic device properties can be controlled by processing conditions such as thermal annealing.<sup>40,41</sup> Fine-tuning of molecular packing is furthermore possible by small changes in the molecular substitution patterns.<sup>42,43</sup> Typically,

Received: August 13, 2017

Revised: October 7, 2017

Published: October 23, 2017



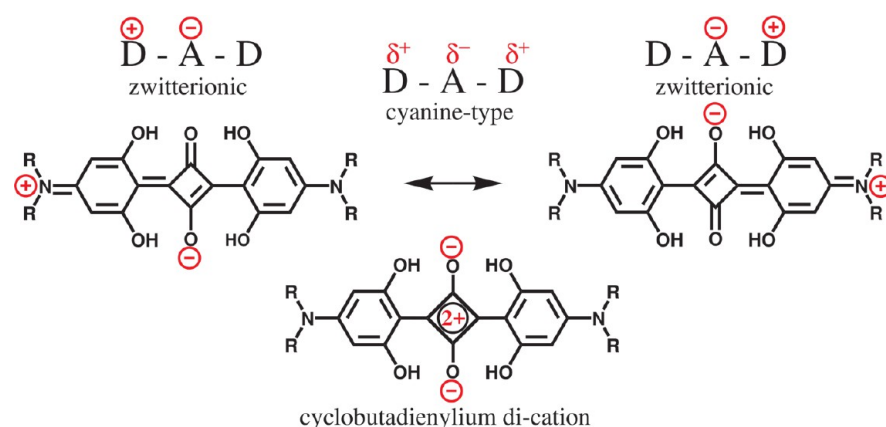


**Figure 1.** Squaraine is a quadrupolar molecule with two resonant, degenerate zwitterionic (betaine-type) states  $D^+A^-D$  and  $DA^-D^+$ , and an energetically different cyanine-type state  $D^{\delta+}A^{\delta-}D^{\delta+}$ . The squaraine also possesses a cyclobutadienylium dication character.<sup>13</sup> If R equals iso-butyl, the formula represents SQIB.

packing is reduced to a molecular dimer picture of H- and J-aggregates (Kasha-aggregates),<sup>44</sup> see Figure 2, with blue-shifted

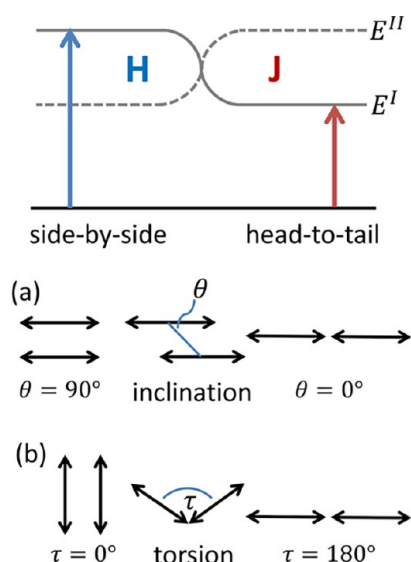


**Figure 2.** Not-to-scale Frenkel exciton band energy diagrams and sketches of the molecular dimer transition dipole moment orientation (Kasha-aggregates). For a side-by-side orientation blue-shifted absorbing H-aggregates form. For a head-to-tail orientation red-shifted absorbing J-aggregates form. A transformation from side-by-side to head-to-tail orientation can happen through (a) inclination described by inclination angle  $\theta$  or (b) torsion described by torsional angle  $\tau$ . If  $\tau$  does not equal  $0^\circ$  or  $180^\circ$ , or more generally speaking, if noncoplanar aligned transition dipole moments of translationally invariant molecules in a primitive unit cell couple, both transitions to the upper ( $E^{II}$ ) and lower ( $E^I$ ) energy levels are allowed simultaneously (Davydov splitting).

and red-shifted absorption, respectively. Excitonic spectral splitting (Davydov splitting)<sup>45</sup> and shifts arise from the mutual orientation of the molecular transition dipole moments and their long-ranged Coulombic interactions resulting in Frenkel excitons.<sup>46,47</sup> For two or more translationally invariant molecules within a primitive crystallographic unit cell, the transition dipole moment alignment can be oblique-angled or twisted. This allows both Davydov components to be present in the absorption spectra simultaneously. They are characterized by the fact that they are polarized mutually perpendicular in the plane of the two

Davydov transition dipoles.<sup>44</sup> For preferential crystallographic alignment in thin films, the projection of the Davydov components can result in an apparent mutual polarization different from  $90^\circ$  depending on the structural properties.<sup>48</sup> Investigations of such pleochroism through optical polarization properties allows for determining the crystallographic unit cell in-plane alignment.<sup>49–51</sup> Recently, Hestand and Spano<sup>52</sup> extended the classical Coulombic Kasha-aggregate picture by short-ranged charge transfer (CT) interactions.<sup>53</sup> Thus, discussion on photophysics of classical molecular aggregates combined with the intermixing CT interaction are revitalized due to the value for rational optoelectronic material design.<sup>52,54–58</sup>

In this paper we show that the dihydroxy anilino squaraine SQIB with a *branched* isobutyl side chain crystallizes both in the bulk as well as in spin-casted thin films into a monoclinic or orthorhombic phase with two or four translationally invariant molecules per unit cell. From the single crystal structures, we infer a Davydov-split H-aggregate for the monoclinic phase and a J-aggregate for the orthorhombic phase, respectively, and picture the projected Davydov components in oriented thin films. We prove this by local, polarization-resolved absorption measurements on the distinct, pleochroic morphological features of the crystallographic phases in spin-casted thin films with varying annealing temperatures. We identify the lower Davydov component to be short-axis polarized, along the in-plane stacking directions of the molecules for the orthorhombic phase, while for the monoclinic phase it is long-axis polarized, perpendicular to the molecular in-plane stacking direction. This contrasts the findings of the Collison group<sup>59–61</sup> for *linear* side chain functionalized dihydroxy anilino squaraines. They all crystallize into triclinic structures with only a single molecule per unit cell, thus not supporting Davydov splitting. Consequently, the origin of the double-peaked absorption spectra must be different. The Collison group identified the short-wavelength peak as H-like aggregate, and the long-wavelength peak as an intermolecular CT interaction of neighboring molecules, which was well supported by theory. Here, we provide, for the first time, a complete correlation of structure, micromorphology, molecular orientation, and local excitonic optical properties of polymorphic SQIB thin films. Thereby, we point out a general trend that simple variation of alkyl side chains combined with variable processing conditions greatly impacts the excitonic properties of anilino squaraine thin films. Together with the ability to locally probe the direction of transition dipole moments, we add value to the

Table 1. Unit Cell Parameters of SQIB Single Crystals

polymorph	<i>a</i> in Å	<i>b</i> in Å	<i>c</i> in Å	$\beta$ in °	<i>Z</i>
P21/ <i>c</i> (monoclinic)	6.1979(2)	16.4874(6)	15.4762(5)	111.248(2)	2
P21/ <i>c</i> by Thompson et al. <sup>70</sup>	6.2034(16)	16.478(4)	14.518(4)	92.406(4)	2
<i>Pbcn</i> (orthorhombic)	15.0453(8)	18.2202(10)	10.7973(6)	90	4
<i>Pbcn</i> by Palomares et al. <sup>72</sup>	15.0473(8)	18.1959(10)	10.7775(6)	90	4

rational design of functional thin films for optoelectronic applications, especially envisioning ultrastrong light–matter interactions.

## ■ EXPERIMENTAL SECTION

**Synthesis and Single Crystal Analysis.** 2,4-Bis[4-(*N,N*-diisobutylamino)-2,6-dihydroxyphenyl]squaraine (SQIB) was purchased from Sigma-Aldrich as well as synthesized in our laboratories according to a known protocol.<sup>62</sup> The commercial SQIB was a macro-crystalline powder and contained several single crystals suitable for structure determination, all forming the orthorhombic phase. Crystals adopting the monoclinic phase were grown from a chloroform solution of the homemade compound by slow evaporation of the solvent.

The single crystal structure of the orthorhombic polymorph was measured with a Bruker AXS Kappa Apex II diffractometer at 120 K using graphite-monochromated Mo- $K\alpha$  radiation ( $\lambda = 0.71073$  Å). Crystal dimensions 0.50 mm  $\times$  0.06 mm  $\times$  0.05 mm, brownish-green with an intense metallic golden luster, C<sub>32</sub>H<sub>44</sub>N<sub>2</sub>O<sub>6</sub>, *M* = 552.69 amu, orthorhombic, space group *Pbcn*, *a* = 15.0453(8) Å, *b* = 18.2202(10) Å, *c* = 10.7973(6) Å, *V* = 2959.8(3) Å<sup>3</sup>,  $\alpha = \beta = \gamma = 90^\circ$ , *Z* = 4, density 1.240 g/cm<sup>3</sup>, absorption coefficient 0.085 mm<sup>-1</sup>, *F*(000) = 1192, 66 666 reflections collected (4335 unique, *R*<sub>int</sub> = 0.0509, completeness 100%, final *R* indices (*I* > 2σ(*I*)) *R*1 = 0.0667, *wR*2 = 0.1254 (all data), GOF = 1.037 for 193 parameters and 0 restraints, largest diff. peak and hole 0.511 e-Å<sup>-3</sup> and -0.242 e-Å<sup>-3</sup>.

The single crystal structure of the monoclinic polymorph was measured with a Nonius KappaCCD diffractometer at 123 K using graphite-monochromated Mo- $K\alpha$  radiation ( $\lambda = 0.71073$  Å). Crystal dimensions were 0.50 mm  $\times$  0.15 mm  $\times$  0.08 mm, C<sub>32</sub>H<sub>44</sub>N<sub>2</sub>O<sub>6</sub>, *M* = 552.69 amu, monoclinic, space group P21/*c*, *a* = 6.1979(2) Å, *b* = 16.4874(6) Å, *c* = 15.4762(5) Å,  $\beta = 111.248(2)^\circ$ ,  $\alpha = \gamma = 90^\circ$ , *V* = 1473.96 Å<sup>3</sup>, *Z* = 2, density 1.245 g/cm<sup>3</sup>, absorption coefficient 0.085 mm<sup>-1</sup>, *F*(000) = 596, 29 420 reflections collected (3550 unique, *R*<sub>int</sub> = 0.0826, completeness 99.8%, final *R* indices (*I* > 2σ(*I*)) *R*1 = 0.0459, *wR*2 = 0.1032 (all data), GOF = 0.911 for 191 parameters and 0 restraints, largest diff. peak and hole 0.217 e-Å<sup>-3</sup> and -0.255 e-Å<sup>-3</sup>.

The structures were solved with SHELXS-97 and then refined with the SHELXL 2013/4<sup>63</sup> for the orthorhombic polymorph and with SHELXL 2014/7<sup>64</sup> for the monoclinic polymorph, respectively. The crystallographic data files can be found online at the Cambridge Crystallographic Data Centre under the CCDC codes 1567104 and 1567209. Unit cell parameters of both structures are also given in Table 1. The single crystal structure data were visualized and analyzed with Mercury 3.9 (Build RC1), available free of charge from [www.ccdc.cam.ac.uk/mercury/](http://www.ccdc.cam.ac.uk/mercury/).<sup>65</sup>

**Thin Film Preparation and Characterization.** Custom-made or commercial SQIB was dissolved in amylene stabilized chloroform (Sigma-Aldrich) to give a 6 or 5 mg/mL solution, respectively. 15 mm  $\times$  15 mm coverslip glasses (Menzel) used as substrates were cleaned in isopropanol. Thin films were prepared by spin-casting 65  $\mu$ L of the solutions onto the coverslip glasses at 1500 rpm for 60 s. The samples were subsequently annealed at 60 °C for 20 min, and at 90 °C, 120 or 180 °C for 2 h on a hot plate. The indicated temperatures were measured at the hot plate surface. Preparation was done in a nitrogen-filled glovebox, while all further characterization of the thin films was carried out under ambient conditions.

Macroscopic, specular UV–vis absorbance spectra were recorded on an Agilent Cary 100 with a custom-made sample holder for supported thin films. The spectra were referenced against air, i.e., not corrected for the absorbance of the glass substrate.

X-ray diffraction (XRD) on thin films in Bragg–Brentano geometry with automatic divergence slit was performed in a PANalytical X'PertPro MPD diffractometer using Cu- $K\alpha$  radiation ( $\lambda = 1.542$  Å), tube set to 40 kV and 40 mA with 10 mm beam mask. Samples were rotated in a sample spinner during measurement to eliminate possible effects from preferential in-plane orientation.

Atomic force microscopy (JPK NanoWizard) was performed in intermittent contact mode (Budget Sensors Tap-300G, resonance frequency 300 kHz, force constant 40 N/m, tip radius <10 nm, and NANOSENSORS SSS-NCH, resonance frequency 330 kHz, force constant 42 N/m, tip radius <5 nm) under ambient conditions and in combination with an inverted optical microscope (Nikon Eclipse TE 300) to image the very same sample region characterized by optical means before.

The anisotropic optical properties of the samples such as birefringence and bireflectance were investigated using several polarized light microscopes: Nikon Eclipse ME-600 epifluorescence microscope, Leica DMRME polarization microscope, and Olympus BX41. To determine the local extinction direction, the samples were rotated in between two crossed polarizers by a Thorlabs PRM1Z8 motorized and computer controlled rotation stage. Images were captured every 5° of rotation by a Pixelink PL-B873-CU camera. From the intensity dependence, the extinction angle was extracted for every image pixel by a discrete Fourier transform;<sup>66–68</sup> see the more detailed description and Figure S4 in the Supporting Information. Images were analyzed with ImageJ.<sup>69</sup>

The linear optical properties of the samples were investigated by using a home-built, polarization-resolved confocal transmission microscope, called spectro-microscope later. The collimated light from a halogen lamp (Fiber Lite DC950, Dolan-Jenner) with a broad spectrum ranging from 450 to 900 nm was linearly polarized using a Glan-Taylor polarizer (PGL12.2, B. Halle Nachf. GmbH) and focused by a Schwarzschild objective (5002-000, NA 0.5, 15 $\times$  magnification, Beck Optronic Solutions) onto the sample surface. The diameter of the light spot on the sample was determined to about 40  $\mu$ m. The transmitted light was collected via a second Schwarzschild objective (5006-000, NA 0.65, 52 $\times$  magnification, Beck Optronics) and imaged onto a pinhole with a diameter of 75  $\mu$ m. The spatial selection in the image plane resulted in a spatial resolution of <1  $\mu$ m. The light was analyzed in a VIS-NIR spectrometer (SP2150 monochromator, Princeton Instruments in combination with a Peltier-cooled CCD camera, Pixis eXcelon 400BR, Princeton Instruments). A thin-film polarizer (colorPol VIS, Codixx AG) implemented in a motor-driven rotation mount with adjustable rotation angle  $\Delta\phi$  was used as an analyzer for the polarization. By additionally raster-scanning the sample through the light spot using a 3D-piezo scanner (P-611.3 Nanocube, Physik Instrumente), polarization-resolved maps of the transmitted spectrum were obtained.

## ■ RESULTS AND DISCUSSION

**Single Crystal Structures and Excitonic Molecular Aggregate Picture.** For SQIB, two polymorphs have been documented in the literature: a monoclinic phase (space group P21/*c*)<sup>70–72</sup> and an orthorhombic phase (space group *Pbcn*).<sup>72</sup> We could confirm the single crystal data, but found slightly different unit cell parameters for the monoclinic crystal. Both polymorphs adopt a herringbone packing and comprise two molecules per unit cell in the monoclinic phase and four in the orthorhombic phase, thus allowing for Coulombic excitonic coupling and spectral features with Davydov splitting. The unit



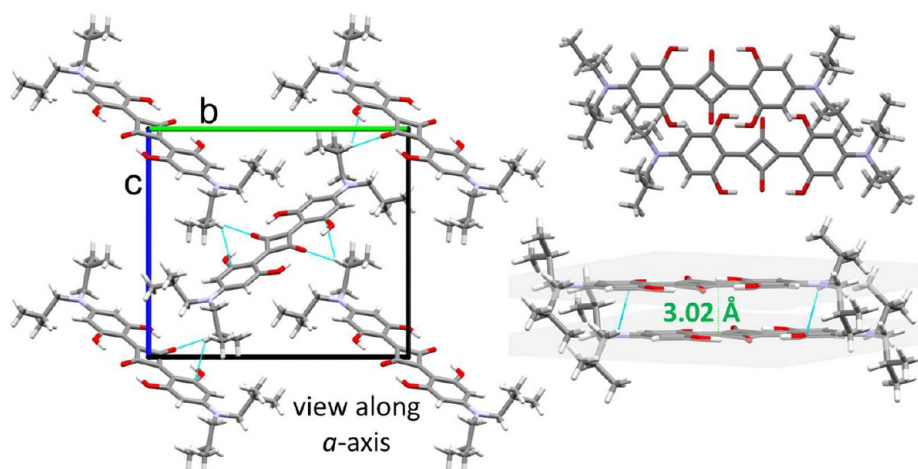


**Figure 3.** Monoclinic polymorph adopts a classical herringbone packing within the crystallographic *bc*-plane and a slipped  $\pi$ -stacking along the *a*-axis. The nonprojected inclination angle  $\theta$  (see Figure 2) of a dimer sandwich is  $58^\circ$ . The stacks form cavities that are filled by the adjacent layer. Short contacts are distances shorter than the sum of van-der-Waals radii marked by light blue lines. The herringbone packing short contacts amount to  $2.56 \text{ \AA}$  for butyl-H to squaric-O and to  $2.80 \text{ \AA}$  for butyl-H to anilino-C. The interplanar distance for the  $\pi$ -stacking is  $3.02 \text{ \AA}$ . The  $\pi$ -stacking short contact from butyl-H to anilino-C is  $2.89 \text{ \AA}$ . Unit cell axes color coding: *b*: green, *c*: blue.

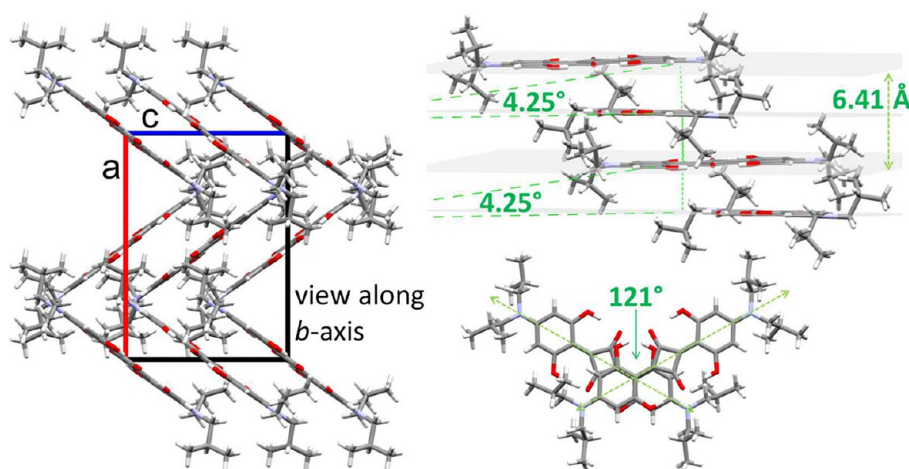


**Figure 4.** Orthorhombic polymorph packs in a cofacial herringbone structural motif appearing as zigzag structure within the crystallographic *ac*-plane. The direction of  $\pi$ -stacking is along the *c*-axis; see also Figure 6d. The consecutive molecules within a stack are rotated toward each other in an alternating manner. The torsional angle amounts to  $121^\circ$ ; see also Figure 2. The neighboring molecules within a stack include an oblique angle of  $4.25^\circ$ . The distance between two coplanar, parallel molecules within a stack is  $6.41 \text{ \AA}$ . Unit cell axes color coding: *a*: red, *c*: blue.

cell parameters of SQIB single crystals including literature values are summarized in Table 1.

The central squaraine core is stabilized by hydrogen bonding resulting in a coplanar arrangement of the squaric- and the anilino-rings. The net molecular C–C bond length suggests a cross-conjugated cyanine-type structure. The bond order of the C–C bond connecting the squaric- and the anilino-ring is closer to a single bond indicating that the molecule also possesses a cyclobutadienylium dication character, see Figure 1. This character is slightly more pronounced for the orthorhombic phase indicated by a minimal longer bond length connecting the squaric- to the anilino-ring. For the monoclinic phase, instead, the quinoidic character of the anilino-rings is more pronounced. The transition dipole moment for the  $S_0 \rightarrow S_1$  molecular transition is along the long molecular axis of the squaraine core.<sup>73–75</sup> To correlate molecular packing and the through space coupling of transition dipole moments within the excitonic dimers, we now follow the molecular dimer picture of Kasha-aggregates, Figure 2.

For a side-by-side orientation of the transition dipoles of each monomer, an H-aggregate with an absorption resonance that is blue-shifted with respect to the monomer absorption forms. For a head-to-tail orientation a J-aggregate with red-shifted absorption relative to the monomer absorption manifests. These are the ideal cases which can transform into each other and eventually show both spectral signatures simultaneously. A transformation from H- to J-type can happen through inclination (inclination angle  $\theta$ ), Figure 2a. At the magic inclination angle  $\theta = 54.7^\circ$  no excitonic splitting occurs. For  $54.7^\circ < \theta \leq 90^\circ$  H-band, and for  $0^\circ \leq \theta < 54.7^\circ$  J-band spectral signatures are visible. If the transformation happens through torsion (torsional angle  $\tau$ ) the dimer absorbance is dominated by a blue-shifted H-band for torsional angles  $\tau < 90^\circ$ , or by a red-shifted J-band for  $\tau > 90^\circ$ .<sup>7</sup> If  $\tau$  does not equal  $0^\circ$  or  $180^\circ$ , both transitions to the upper ( $E^{\text{II}}$ ) and lower ( $E^{\text{I}}$ ) energy levels are allowed simultaneously. Generally speaking, this is the case if noncoplanar aligned transition dipole moments of two or more translationally invariant molecules in a primitive unit cell couple. The energetic

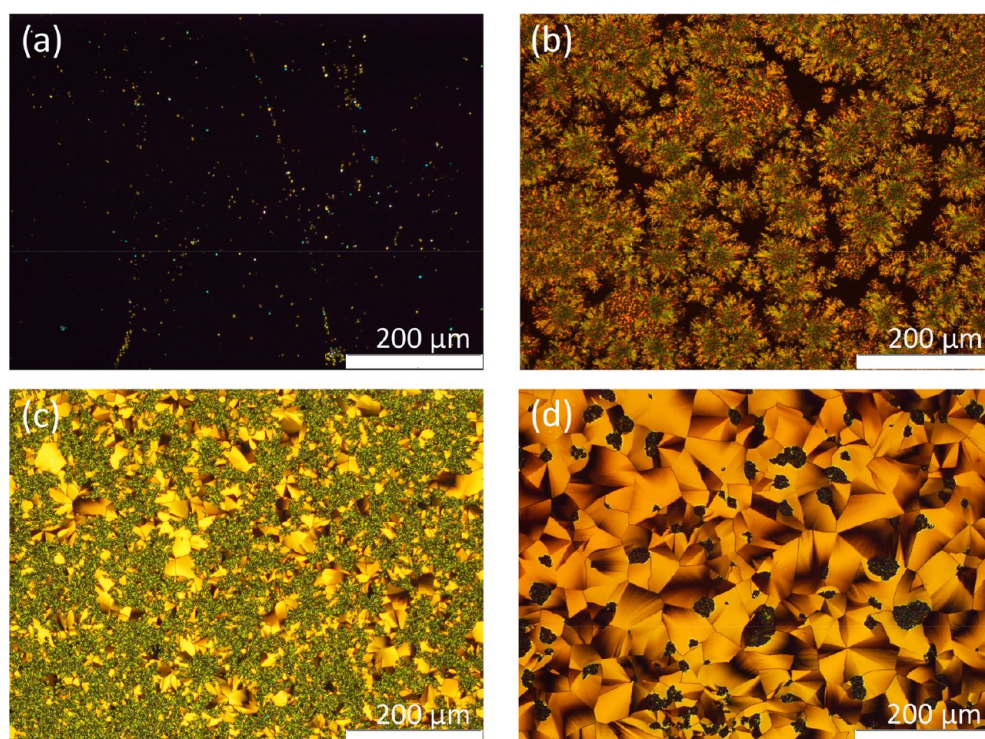


**Figure 5.** Optical microscopy images between crossed polarizers of spin-coated SQIB thin films annealed at (a) 60 °C, (b) 90 °C, (c) 120 °C, and (d) 180 °C.

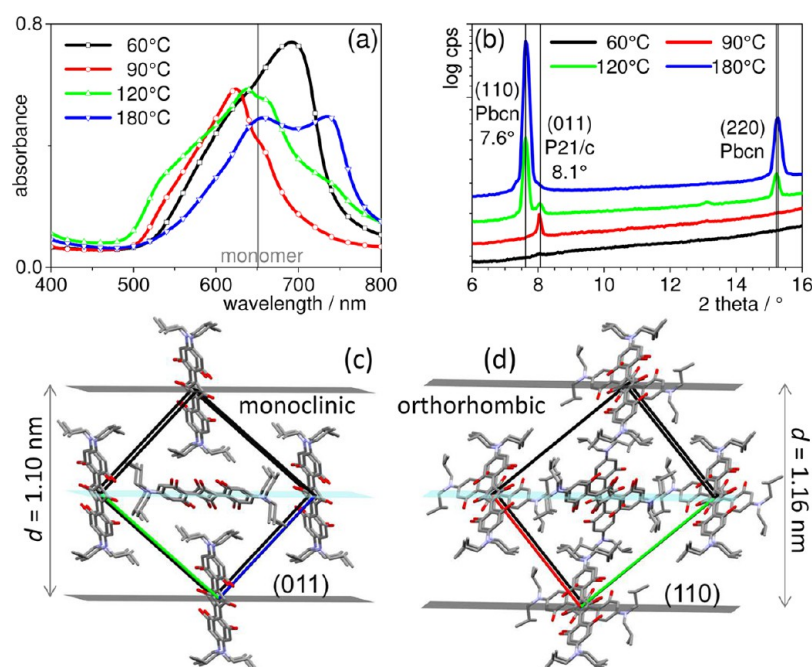


**Figure 6.** (a) Absorbance spectra and (b) XRD patterns of spin-coated SQIB thin films annealed at different temperatures as indicated. The vertical gray line in (a) indicates the maximum of the sharp absorbance band of SQIB dissolved in chloroform. Structure picture of (c) the monoclinic phase with the (011) plane horizontally aligned and view almost along the crystallographic *a*-axis, which is the molecular stacking direction, and (d) the orthorhombic phase with the (110) plane horizontally aligned and view almost along the crystallographic *c*-axis, which is the molecular stacking direction. Axes color coding: *a*: red, *b*: green, *c*: blue.

difference between the upper and lower energy levels is called Davydov splitting.<sup>45</sup> The upper Davydov component (UDC) at higher energy (blue-shifted wavelength) results from the vector difference of the transition dipole moments, while the lower Davydov component (LDC) at lower energy (red-shifted

wavelength) is the vector sum of the transition dipole moments. The overall spectral position of the double bands relative to the monomer absorption band can be totally blue- or red-shifted depending on whether the dimer structure resembles more an H-aggregate or a J-aggregate assembly.<sup>76,77</sup> Depending on the



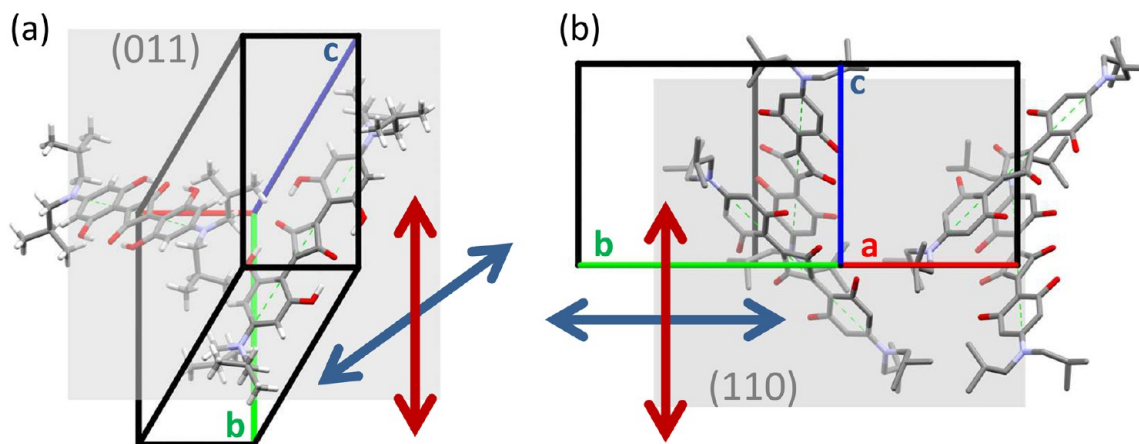


**Figure 7.** Projected in-plane polarization directions of the two Davydov components are sketched for (a) the monoclinic phase (H-aggregate) and (b) the orthorhombic phase (J-aggregate). The LDC is indicated by a red arrow and the UDC by a blue arrow. In (a) LDC = 615 nm points along the *b*-axis (perpendicular to molecular stacking direction), and UDC = 540 nm points along a direction rotated by approximately 56°. See Figure 10 for peak assignment. In (b) LDC = 730 nm is along the crystallographic *c*-axis (molecular stacking direction), and UDC = 640 nm is along the projection of the *b*-axis onto the (110) plane. See Figure 11 for peak assignment.

extent of intermolecular coupling vibronic replicas are present in the absorbance spectra. The distribution of oscillator strength is characteristic for the aggregate type: In H-aggregates, the oscillator strength of the lowest energy vibronic peak ((0–0)-transition) *decreases* relative to the first sideband ((0–1)-transition) with increasing intermolecular coupling whereas in J-aggregates the oscillator strength of the (0–0)-transition *increases* relative to the first vibronic progression ((0–1)-transition).<sup>47,78</sup> This is also valid if a Davydov splitting is present in the absorbance spectra.<sup>79</sup>

The molecular packing of SQIB is shown in Figure 3 for the monoclinic crystal and in Figure 4 for the orthorhombic crystal. The monoclinic polymorph adopts a classical herringbone packing within the crystallographic *bc*-plane and a slipped and inclined  $\pi$ -stacking along the *a*-axis. The stacks form cavities that are filled by the adjacent layer. All molecules within a stack show parallel and coplanar ordering. The aromatic plane distance is 3.02 Å; short contact between two stacked molecules is an H-interaction from an isobutyl side chain hydrogen to an aromatic carbon within the anilino-ring and amounts to 2.89 Å. The short contact between adjacent stacks amounts to 2.56 Å for butyl-H to squaric-O and to 2.80 Å for butyl-H to anilino-C. Thus, the interstack contacts are shorter than the intra- $\pi$ -stack contacts. This is indicative of electronic interstack coupling even though the butyl-chains are not connected to the  $\pi$ -conjugation. Such interstack couplings between translationally invariant molecules can be expressed as Davydov splitting in the absorption spectra. The packing of the monoclinic polymorph appears as H-aggregate dimer due to the side-by-side orientation of slipped but coplanar neighboring molecules within a stack. The *nonprojected* inclination angle of a dimer sandwich is determined to be  $\theta = 58^\circ$ , which is valid for blue-shifted spectral signatures of an H-aggregate, Figure 2. Note that the projection of the inclination angle would lead to a different conclusion.

In the orthorhombic phase the stacking can be understood as two interdigitating stacks rotated by  $121^\circ$  against each other. The aromatic plane distance within a stack of aligned, parallel molecules is 6.41 Å. This means that neighboring stacked molecules are rotated in an alternating manner. In words of Kasha molecular aggregates, the packing of the orthorhombic polymorph can be understood as head-to-tail oriented ordering

with a torsional angle  $\tau > 90^\circ$ , which should result in a red-shifted absorbing J-aggregate, Figure 2. The aromatic planes of two stacked molecules are not parallel but tilted by  $4.25^\circ$ . This oblique orientation of the neighboring molecules allows for a Davydov-splitting. The existence of short herringbone contacts between neighboring stacks indicates that interstack couplings also play a role for the overall electronic coupling, and thus appearance and polarization properties of the Davydov components.

**Correlation of Structure, Morphology, Molecular Orientation, and Excitonic Optical Properties in Polymorphic Thin Films.** Optical microscopy images of spin-casted SQIB thin films annealed at different temperatures are depicted in Figure 5, the corresponding macroscopic absorbance spectra and XRD patterns are graphed in Figure 6a,b, respectively.

Annealing at  $60^\circ\text{C}$  did not initiate noticeable crystallization of the film, and thus, the microscope image between crossed polarizers appears dark apart from a few bright crystallization seeds, Figure 5a. This was also similar for nonannealed thin films (not shown here). As expected, such thin films were XRD-silent, black line in Figure 6b. For such an amorphous sample, the absorbance was a broad hump centered around 690 nm with a shoulder roughly at 620 nm, Figure 6a, black squared curve. Such samples showed the tendency to age within a few weeks, see Figure S1 in the Supporting Information.

Increasing the temperature and duration for the annealing procedure resulted in birefringent and bireflectant crystalline samples, which are stable for months to years. For annealing at  $90^\circ\text{C}$  sunflower-like structures became visible, Figure 5b, consisting of radially aligned fibrous structures. The absorbance changed to a rather sharp peak around 620 nm and two shoulders, one at higher energy (540 nm) and one at lower energy (650 nm), red circled curve in Figure 6a. This sunflower sample consisted of the monoclinic polymorph with the (011) plane (or (01 $\bar{1}$ ) together with their mirror faces) parallel to the substrate indicated by the diffraction peak at  $2\theta = 8.1^\circ$ , red pattern in Figure 6b. Note that these planes are equivalent in out-of-plane XRD recordings, but due to low symmetry of the monoclinic system, the unit cell and consequently molecular in-plane orientation is mirror-inverted at the in-plane oriented *a*-axis on the surface.<sup>80</sup> Further gradual increase of the annealing temperature broadened the spectrum

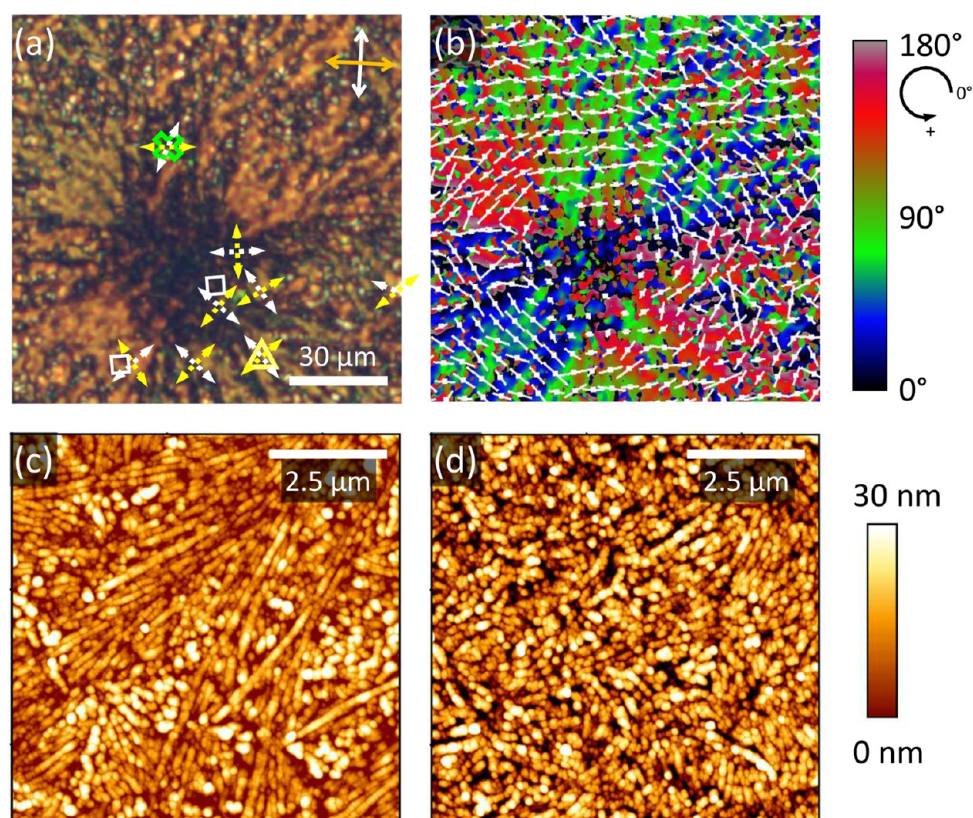


**Figure 8.** (a) Polarized light microscopy image (transmission, polarizer, and analyzer directions marked by a white and orange arrow in the upper right corner, respectively) of a sunflower-like structure. The green cross and yellow triangle mark positions of polarized absorbance spectra shown in Figure 10b. Dashed white and yellow arrows indicate the direction where absorption at  $\lambda = 540$  nm and  $\lambda = 615$  nm is maximum, respectively. Polarization analysis of the sunflower. Short white lines designate an extinction direction. Panels (c) and (d) corresponding AFM images of the sunflower-like texture, demonstrating the submicron fiber-like structures. The positions of the AFM images are marked in (a) by white squares. The image in (d) has been obtained closer to the center of the sunflower, the one in (c) at the periphery.

(120 °C, green triangled curve), ending in a red-shifted spectrum with a double-hump structure (180 °C, blue triangled curve), Figure 6a. The humps appeared at approximately 650 and 730 nm. The microscopy images, Figure 5c,d, show the growth of golden platelets between the sunflower-like texture, ending in a sample completely consisting of such golden platelets apart from a few dewetted spots (dark areas in the image). Note that the colors are interference colors arising from the birefringence of the thin film. Without polarizers all features showed a blue-greenish color in transmission. The gradual change in brightness within a platelet and abrupt change at platelet boundaries stem from different in-plane rotational domains. XRD identified the golden platelets as the orthorhombic polymorph with the (110) plane (or the equivalent  $(1\bar{1}0)$  plane together with the mirror faces) parallel to the substrate indicated by a diffraction peak at  $2\theta = 7.6^\circ$ , blue line in Figure 6b. Also the higher order (220) peak was visible, suggesting a strong preferential out-of-plane ordering. Consequently, the 120 °C sample with a mixture of sunflowers and platelets, visible in the microscopy image Figure 5c, showed diffraction peaks of both polymorphs, green line in Figure 6b. The broad absorption of this sample therefore stemmed from the superposition of the absorbance of the two morphological features, green triangles in Figure 6a.

Figure 6c,d visualizes the molecular orientation for both phases based on the single crystal structures relative to the surface from a side view perspective. For the monoclinic phase the crystallographic  $a$ -axis is parallel to the surface, while for the orthorhombic phase this is the case for the crystallographic  $c$ -axis.

Thus, in both cases the respective unit cell short axis, which is the molecular stacking direction, is parallel to the surface, but with yet nondefined in-plane orientation.

We now want to correlate the projected unit cell axes directions onto the crystallographic plane being parallel to the surface, with the transition dipole moment directions of the projected Davydov components. For this, we depict the two inequivalent molecules of the monoclinic structure when viewed perpendicular to the crystallographic (011) plane, Figure 7a, as well as the two pairs of translationally invariant molecules within the orthorhombic structure with view perpendicular to the crystallographic (110) plane, Figure 7b. Considering the transition dipole moments of a single molecule to be along the long molecular axis, we can calculate the vector sum and difference resulting in the transition dipole moments of the LDC and UDC, respectively. For clarity, we show sketches of the graphical vector addition/subtraction in the Supporting Information, see Figures S2 and S3.

Calculating the projected vector sum and difference of the two translationally invariant molecules within the monoclinic unit cell, see Figure 7a, we find an angle of approximately  $56^\circ$  between the two projected Davydov components. The sum and thus LDC are along the long  $b$ -axis and consequently along the projection of the  $b$ -axis onto the (011) (or  $(0\bar{1}\bar{1})$ ,  $(01\bar{1})$ ,  $(0\bar{1}1)$ ) plane, which was found to be parallel to the surface. This means that LDC is polarized *perpendicular* to the short axis of the unit cell which is the in-plane *stacking direction* of the molecules. The vector difference and thus UDC is in the projection onto the



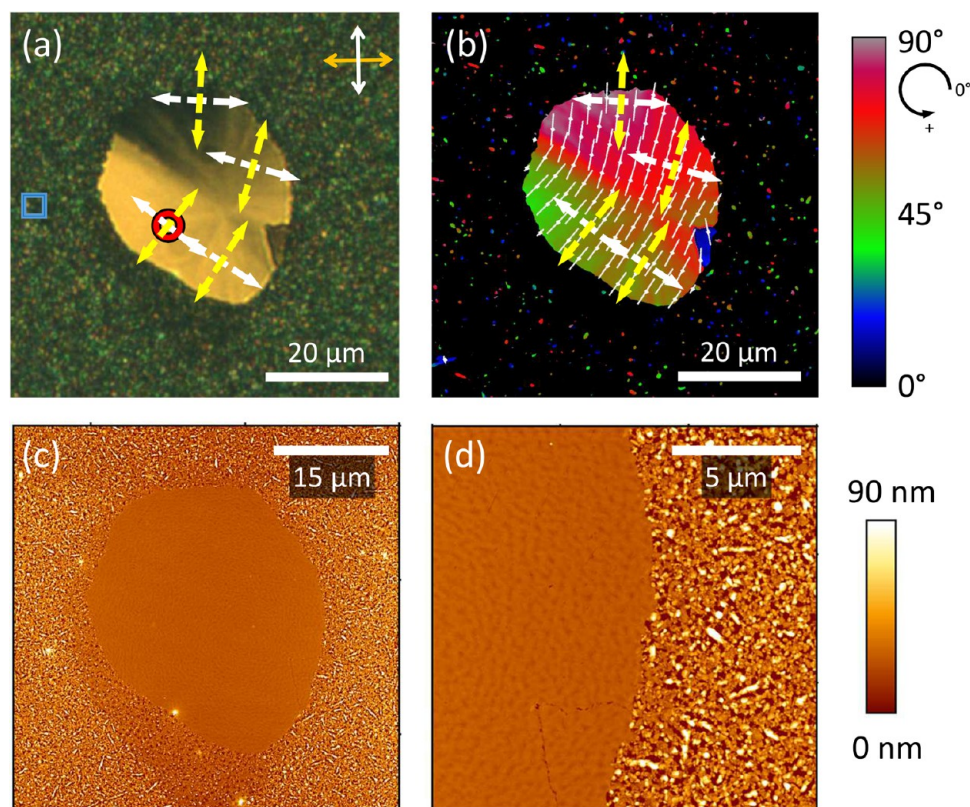


**Figure 9.** (a) Polarized light microscopy image (transmission, polarizer, and analyzer directions marked by a white and orange arrow in the upper right corner, respectively) of a single SQIB platelet. The blue square and red circle mark positions of polarized absorption spectra shown in Figure 11. (b) Polarization analysis of the platelet. The color code together with short white lines mark a local extinction direction. Dashed white arrows indicate the direction where absorption at  $\lambda = 730$  nm is maximum, dashed yellow arrows the same for  $\lambda = 640$  nm. Panels (c) and (d) corresponding AFM images of the platelet.

plane along a direction rotated by approximately  $56^\circ$ . Other examples for *b*-axis polarization of the LDC component from H-type aggregating molecules with monoclinic unit cells can be found for thiophene-phenylene co-oligomers<sup>81</sup> and penta-cene<sup>49,82</sup> as a representative for the acene family. Since the absorbance of the monoclinic polymorph shows three peaks, red circled line in Figure 6a, the assignment of UDC and LDC to the spectral positions requires polarization resolved measurements.

For the orthorhombic phase, Figure 7a, we consider all four molecules to contribute equivalently to obtain only two main Davydov components to match the double-hump structure of the absorption profile, blue triangled line in Figure 6a. Thus, *intra*-stack as well as *inter*-stack Coulombic couplings play an equal role to describe the excitonic properties as anticipated from the crystal structure. The vector sum is along the short *c*-axis, which is therefore the polarization direction of the LDC at 730 nm. This means that LDC is polarized *along* the short axis of the unit cell which is the in-plane *stacking* direction of the molecules. The vector difference points along the *b*-axis, which is therefore the polarization direction of the UDC absorbing at 640 nm. In the projection onto the (110) plane the UDC is along the projected *a*-*b*-axes direction. Thus, the Davydov components are polarized mutually perpendicular in the crystallographic plane parallel to the substrate. For pleochroic perylene diimide crystals with a similar twisted sandwich stacking of four pairs of translationally invariant molecules within a monoclinic unit cell, only the coupling of the sandwiched nearest neighbors was considered.<sup>50</sup> Thus, in that case the *intra*-stack coupling was dominant, and also charge transfer coupling in addition to the

Coulombic coupling was considered to fully reproduce the absorbance spectra. However, the LDC was found to be short (= stacking) axis polarized just as for our orthorhombic platelets.

We can conclude so far that the overall absorbance profiles are coincident with the considerations based on the single crystal structures: the monoclinic sunflowers are H-aggregates with a blue-shifted absorbance profile, and the orthorhombic platelets are J-aggregates with a red-shifted profile. Both structures have the appropriate packing to support Davydov splitting. Now we aim to clarify and confirm the nature of the signatures within the respective absorbance spectra and to obtain a more detailed picture of the in-plane orientation of the crystalline domains. For this we applied cross-polarized light microscopy and polarized spectro-microscopy. The former probes the birefringence/bireflectance and therefore refers to the refractive index of the material. The latter measures polarized absorbance and therefore addresses the pleochroic properties of the sample, which is evident for a Davydov splitting.

A sunflower is imaged in Figure 8a between crossed polarizers. Accordingly a characteristic single platelet with an adjacent amorphous area appearing brownish, embedded in a polycrystalline surrounding appearing green, was chosen, Figure 9a. The white and orange arrows in the upper right corner of Figures 8a and 9a mark the polarizer and analyzer directions, respectively. The colors are similar for observation in transmission and reflection. Rotating the platelet sample does neither change the appearance of the greenish surrounding nor the color of the platelet, but alters the parts where the platelet appears dark, i.e., the local extinction direction. For the sunflowers, the colors



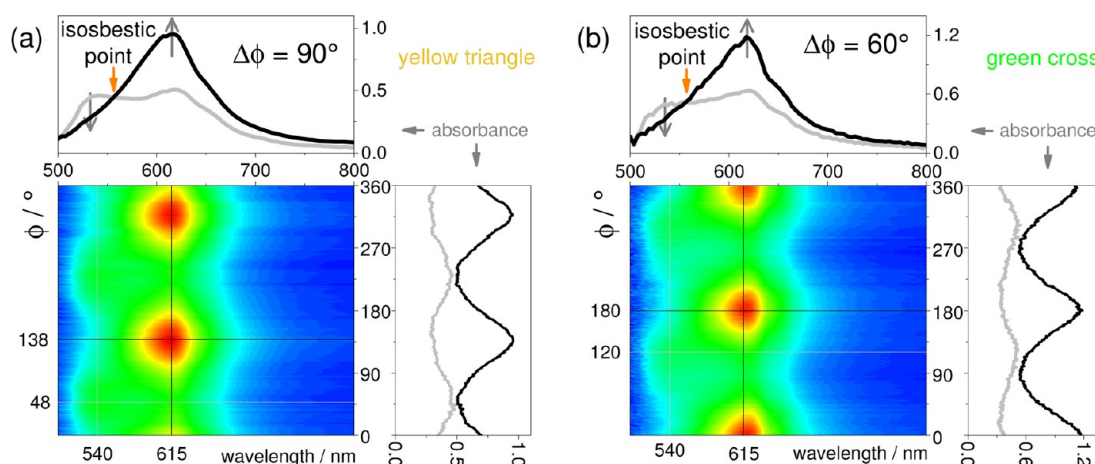


**Figure 10.** Polarized spectro-microscopy recordings of a sunflower sample at two different positions, (a) yellow triangle and (b) green cross indicated in Figure 8a.

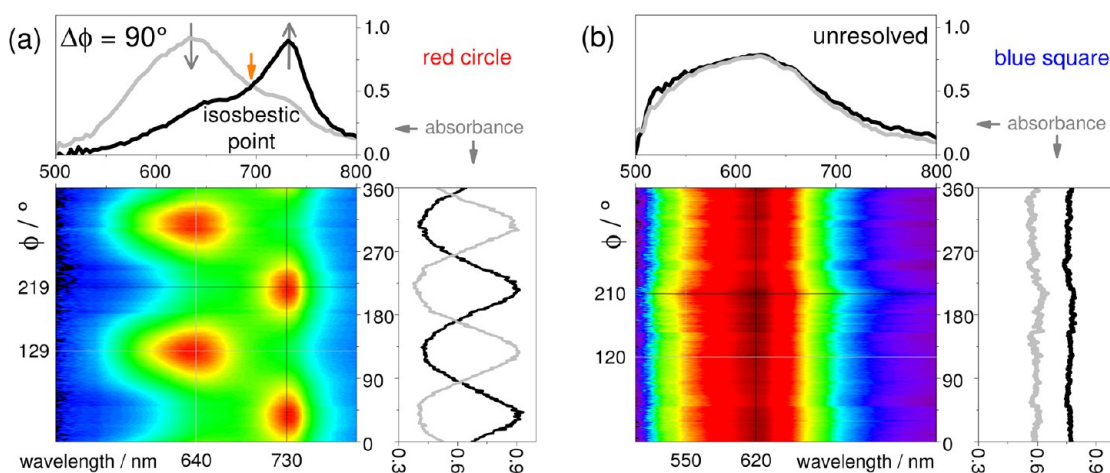


**Figure 11.** Polarized spectro-microscopy recordings of (a) platelet at the position marked by the red circle, and of (b) polycrystalline area at the position marked by the blue square in Figure 9a.

alternate between red and green passing black. The morphology consists of submicron wide fibers, aligned radially with respect to the center, Figure 8c, together with cluster-like aggregates and less well-defined areas. In the center of the sunflower, Figure 8d, fibers are shorter and not mutually aligned in a parallel fashion, resulting in an area with only a small amount of birefringence. Obviously, a sunflower is of polycrystalline nature with small domain sizes. The dark color of the wedge on the right side within the platelet, Figure 9a, originates from a different in-plane crystallographic orientation of that wedge. The grain boundaries are visible in the atomic force microscopy (AFM) images, Figure 9c,d. Obviously, the rest of the platelet is not single crystalline. Even if no sharp grain boundaries are noticeable, there is a gradual change in in-plane orientation. Animated images of rotating samples between crossed polarizers are provided in the Supporting Information, Figure S4.

The analysis of the local extinction angles allows the assignment of local in-plane orientation of the crystalline domains. The local extinction angles, i.e., the angle where at this point the transmission is smallest, are visualized in Figures 8b and 9b by the color code and also by short white lines. The length of the lines is a measure for the amount of birefringence, averaged over an area covering half of the distance between neighboring lines. For monoclinic crystals only one of the indicatrix axes is

fixed to the unit cell coordinate system; i.e., one of the indicatrix axes is along the crystallographic *b*-axis. Since for (011) and the other three possible contact planes the *a*-axis but not the *b*-axis is parallel to the surface, the extinction direction is in general not along a projection of the crystallographic axes onto the surface. In order to determine the orientation of the extinction angles with respect to the projected crystallographic axes, additional information about the acute bisectrix and the angle between the two optic axes  $2V$ , and the angular relationships between indicatrix axes and crystallographic axes are needed.<sup>83,84</sup> Unfortunately, all these are not known for the monoclinic SQIB polymorph. Furthermore, the distribution of birefringence extinction angles is delicate for the sunflowers due to their lacy texture and polycrystalline nature. One of the extinction directions is usually radially aligned, the other one, which is emphasized in Figure 8b, consequentially tangential. For orthorhombic crystal systems, such as the platelets, the biaxial indicatrix axes are all parallel to the crystallographic axes. Since the (110) plane, and consequently the *c*-axis, is parallel to the surface, extinction is observed if the *c*-axis points along one of the two polarizer axes.<sup>83,85,86</sup> This is also the case for the three other possible contact planes. The other polarizer axis denotes the direction of the projected *a*-*b*-axes.

From such basic polarization microscopy measurements alone, it cannot be decided which polarizer direction corresponds to which unit cell axis. To further elucidate the in-plane orientation of the unit cell and to locate the Davydov bands, we take advantage of the pleochroic properties of the platelet and the sunflower and record single-polarizer local transmission spectra. From this, the local absorbance has been calculated. Positions of interest are marked for each sample: For the sunflower in Figure 8a a green cross and a yellow triangle, and in Figure 9a a spot on the platelet (red circle) and a spot within the polycrystalline area (blue square). A series of polarized absorption spectra with rotated polarizer at these selected positions are plotted in Figure 10 for the sunflower sample, and in Figure 11 for the platelet sample. Sets of absorbance spectra depending on the rotation angle are also shown for both polymorphs in the Supporting Information Figure S5.

In the case of the sunflower-like morphology, no clear polarized spectro-microscopy recording could be obtained due to resolution limitation of the microscope. In the center of the sunflower, absorption shows only a single band at 615 nm and is almost isotropic, whereas in the birefringent part we could identify two Davydov-split bands which are at 540 nm (UDC) and at 615 nm (LDC), Figure 10, due to its pleochroic behavior. Note that the LDC was found to peak rather sharply at 620 nm in the macroscopic UV–vis measurement, Figure 6a. Since it is typical for H-aggregates that the lowest energy vibronic peak, i.e., (0–0), decreases in oscillator strength in favor of the first sideband,<sup>78,79</sup> we suggest the peaks at 615 and 540 nm to be the Davydov-split (0–1) vibronic progression. One could expect the UDC (540 nm) to be more intense than the LDC (615 nm), which is apparently not the case. This might be because the LDC projects stronger onto the crystallographic plane being parallel to the substrate,<sup>50</sup> and/or to a spectral superposition of the (0–1)-LDC (615 nm) with a not resolved (0–0)-UDC. For the latter case, consequently, the shoulder at lower energy at 650 nm, hardly noticeable in the spectro-microscope, is most likely the (0–0)-LDC transition. Then, the (0–1)-LDC (615 nm) and the (0–0)-LDC (650 nm) are expected to have the same polarization properties. And in fact, for these two peaks at 615 and 650 nm, no difference in polarization orientation is visible in Figure 10. However, we are aware that this is just a phenomenological assignment, and full clarity requires support by quantum mechanical calculations.

Considering the polarization properties of the proposed (0–1)-UDC (540 nm) and (0–1)-LDC (615 nm) bands, we found a clear dichroic behavior. In most cases, we found a polarization angle difference of  $\Delta\phi = 90^\circ$  between the two absorption bands, but other angle differences were also observed. The expected  $56^\circ$  angle, Figure 7b, was a rare case. The sum and thus LDC at 615 nm are along the crystallographic *b*-axis and consequently along the projection of the *b*-axis onto the contact plane. The vector difference and thus UDC at 540 nm, projected onto the (011) plane, is rotated by approximately  $56^\circ$ . The reason for the dominantly apparent angle of  $90^\circ$  is probably caused by the spatial summation over neighboring submicron fibers having one of the four different contact planes, which bear the *b*-axis as in-plane-mirror-axis, twinning within single fibers, or fibers with a certain random in-plane orientation within the detection area of the spectro-microscope. Thus, the sum of UDC components appeared under a  $90^\circ$  orientation angle relative to the LDC component. Consequently, we can only identify the orientation of the *b*-axis (LDC, 615 nm). The maximum absorption along the *b*-axis (dashed yellow arrow) coincides well with the

tangential extinction direction from the birefringence measurements, marked by short white lines in Figure 8b. The alignment of the *b*-axis is predominantly perpendicular to the radial direction of a sunflower. From monitoring the aging of an amorphous sample by AFM, see Supporting Information Figure S1, we know that a sunflower grows radially outward from a center seed. Growth is typically in the direction of the short unit cell axis thus along the molecular stacking direction, which is for the sunflower indeed perpendicular to the projected *b*-axis, i.e., in the radial direction. A color shift due to an additional waveplate in the polarization microscope suggests that this corresponds to the slow axis, i.e., the axis with the higher index of refraction.

For the platelets it was straightforward to analyze the spectro-microscopy recordings. The two bands of the platelet showed a  $90^\circ$  out of phase behavior, Figure 11a. If the peak at 640 nm was at maximum intensity, the peak at 730 nm was at minimal intensity, and the situation was reversed upon rotating the polarizer by  $90^\circ$ . The local extinction direction is parallel/perpendicular to the direction where absorption is at its maximum, indicated by dashed white and yellow arrows in Figure 9b. An isosbestic point, i.e., a point of constant intensity where all spectra cross, was visible indicating that both bands belong to the same aggregate species. From that we can confirm that there actually is a Davydov-splitting present in the absorption spectra as we estimated from the analysis of the molecular packing within the crystallographic plane parallel to the substrate, Figure 7a. Note that the upper Davydov component (UDC) was found to peak at 640 nm in the spectro-microscope, while the macroscopic UV–vis measurement, Figure 6a, detected approximately 650 nm. The measured values for the lower Davydov component (LDC) were in good agreement.

## CONCLUSIONS AND OUTLOOK

We have characterized the relation between structure, micro-morphology, and optical properties of polymorphic thin film samples from an anilino squaraine with branched alkyl side chains (SQIB). Two crystalline phases could be identified, a monoclinic structure manifesting in thin films as lacy sunflower-like morphology with blue-shifted spectral signatures of an H-aggregate as well as an orthorhombic phase with platelet-like morphology and red-shifted J-aggregate features. Both polymorphs adopt herringbone packing, the monoclinic phase comprising coplanar and slipped molecular stacks, and the orthorhombic phase exhibiting oblique angled molecular stacks with alternating twist. The overall spectral shifts as well as the Davydov-splitting can be deduced from the single crystal structures. Both SQIB polymorphs contain translationally invariant molecules per unit cell and thus support Davydov-split Frenkel exciton spectral features. For the excitonic coupling intrastack and interstack interactions contribute equally. In contrast, anilino squaraines with linear alkyl side chains, thoroughly investigated by the Collison group,<sup>59–61</sup> do not support Davydov splitting since all compounds adopt triclinic crystal structures with only a single molecule per unit cell. Consequently, they interpreted the double peak spectral signatures as H- and CT-band, respectively, which is well supported by theory. However, polarization properties of such thin film samples have not been investigated so far, which is therefore of relevance for future investigations.

In spincoated SQIB thin films, the formation of the monoclinic sunflowers and the orthorhombic platelets can be controlled by thermal annealing. Both phases adopt a strongly preferred out-of-



plane orientation with their molecular stacking directions parallel to the surface, while the in-plane orientation is rather random. The identification of the unit cell orientation through optical polarization properties is straightforward for the orthorhombic platelets, while it can only partly be unwind for the monoclinic sunflowers. Here, the fibrous texture combined with the possible formation of different mirrored twin domains is not resolvable within the optical microscopes. We can identify the lower Davydov component to be *c*-axis polarized for the orthorhombic J-type platelets, while for the monoclinic H-type sunflowers it is *b*-axis polarized. This means that the LDC is short-axis polarized along the molecular stacking direction for the J-aggregate contrasting the long-axis polarization perpendicular to the molecular stacking direction of the LDC for the H-aggregate. With that, we provide knowledge of the complete molecular packing and alignment determining the excitonic properties combined with the ability of controlled preparation through variation of processing conditions. So far, we have only investigated simple solution processing on plain glass substrates; for the future we will extend the studies to vapor deposition on various substrates. Furthermore, we think that our findings together with those by the Collison group point out a general trend in the sense of how simple variation of the alkyl side chains steers the aggregation and resulting excitonic properties. Anilino squaraines with branched alkyl side chains are prone to forming classical Kasha-aggregates with Frenkel exciton spectral signatures, while linear alkyl side chains give rise to a different packing allowing for sizable short-ranged CT interaction. In addition, the crystallization can be controlled via simple thermal treatment of the thin films.

Altogether, with our present study we provide fundamental knowledge of steerable excitonic molecular interactions for an application relevant model component. This will most likely pave the way for future investigation of more complex, but still fundamental, phenomena such as charge-transfer dynamics and singlet fission as well as ultrastrong light–matter interactions. Such understanding, in turn, will give rise to advanced rational design of functional organic thin films from the nano- to the macro-scale for optoelectronic applications.

## ■ ASSOCIATED CONTENT

### ■ Supporting Information

The Supporting Information is available free of charge on the ACS Publications website at DOI: [10.1021/acs.cgd.7b01131](https://doi.org/10.1021/acs.cgd.7b01131).

AFM images monitoring the aging of amorphous samples; sketches of the graphical vector summation/subtraction of the projected molecular transition dipole moments for the monoclinic and the orthorhombic polymorph; spectro-microscopy recording polarized absorption spectra depending on polarizer angle (PDF)

Bireflectance movies of platelet and sunflower rotated between crossed polarizers (AVI1, AVI2)

### Accession Codes

CCDC 1567104 and 1567209 contain the supplementary crystallographic data for this paper. These data can be obtained free of charge via [www.ccdc.cam.ac.uk/data\\_request/cif](http://www.ccdc.cam.ac.uk/data_request/cif), or by emailing [data\\_request@ccdc.cam.ac.uk](mailto:data_request@ccdc.cam.ac.uk), or by contacting The Cambridge Crystallographic Data Centre, 12 Union Road, Cambridge CB2 1EZ, UK; fax: +44 1223 336033.

## ■ AUTHOR INFORMATION

### Corresponding Author

\*E-mail: [manuela.schiek@uni-oldenburg.de](mailto:manuela.schiek@uni-oldenburg.de).

### ORCID

Frank Balzer: 0000-0002-6228-6839

Arne Lützen: 0000-0003-4429-0823

Martin Silies: 0000-0002-3704-2066

Manuela Schiek: 0000-0002-0108-2998

### Notes

The authors declare no competing financial interest.

## ■ ACKNOWLEDGMENTS

Discussion with G. Witte, University of Marburg, have been inspiring for the data evaluation. We are indebted to J. Parisi for his shared-lab policy, providing access to excellent lab facilities.

## ■ REFERENCES

- (1) Sreejith, S.; Carol, P.; Chithra, P.; Ajayaghosh, A. *J. Mater. Chem.* **2008**, *18*, 264–274.
- (2) Beverina, L.; Sassi, M. *Synlett* **2014**, *25*, 477–490.
- (3) Tristani-Kendra, M.; Eckhardt, C. *J. Chem. Phys.* **1984**, *81*, 1160–1173.
- (4) Tristani-Kendra, M.; Eckhardt, C.; Bernstein, J.; Goldstein, E. *Chem. Phys. Lett.* **1983**, *98*, 57–61.
- (5) Ashwell, G.; Bahra, C.; Brown, G. S.; Hamilton, D.; Kennard, C.; Lynch, D. *J. Mater. Chem.* **1996**, *6*, 23–26.
- (6) Terenziani, F.; Painelli, A.; Katan, C.; Charlot, M.; Blanchard-Desce, M. *J. Am. Chem. Soc.* **2006**, *128*, 15742–15755.
- (7) Sanyal, S.; Painelli, A.; Pati, S. K.; Terenziani, F.; Sissa, C. *Phys. Chem. Chem. Phys.* **2016**, *18*, 28198–28208.
- (8) Moreshead, W. V.; Przhonska, O. V.; Bondar, M. V.; Kachkovski, A. D.; Nayyar, I. H.; Masunov, A. E.; Woodward, A. W.; Belfield, K. D. *J. Phys. Chem. C* **2013**, *117*, 23133–23147.
- (9) Ceymann, H.; Rosspeintner, A.; Schreck, M. H.; Mützel, C.; Stoy, A.; Vauthey, E.; Lambert, C. *Phys. Chem. Chem. Phys.* **2016**, *18*, 16404–16413.
- (10) Yuan, L.; Lin, W.; Zheng, K.; He, L.; Huang, W. *Chem. Soc. Rev.* **2013**, *42*, 622–661.
- (11) Jenkins, R.; Burdette, M. K.; Foulger, S. H. *RSC Adv.* **2016**, *6*, 65459–65474.
- (12) Avirah, R. R.; Jayaram, D. T.; Adarsh, N.; Ramaiah, D. *Org. Biomol. Chem.* **2012**, *10*, 911–920.
- (13) Law, K. Y. *Chem. Rev.* **1993**, *93*, 449–486.
- (14) Schulz, M.; Mack, M.; Kollege, O.; Lützen, A.; Schiek, M. *Phys. Chem. Chem. Phys.* **2017**, *19*, 6996–7008.
- (15) Chen, G.; Sasabe, H.; Igarashi, T.; Hong, Z.; Kido, J. *J. Mater. Chem. A* **2015**, *3*, 14517–14534.
- (16) Brück, S.; Krause, C.; Turrissi, R.; Beverina, L.; Wilken, S.; Saak, W.; Lützen, A.; Borchert, H.; Schiek, M.; Parisi, J. *Phys. Chem. Chem. Phys.* **2014**, *16*, 1067–1077.
- (17) Spencer, S.; Cody, J.; Mixture, S.; Cona, B.; Heaphy, P.; Rumbles, G.; Andersen, J.; Collison, C. *J. Phys. Chem. C* **2014**, *118*, 14840–14847.
- (18) Mayerhöffer, U.; Deing, K.; Größ, K.; Braunschweig, H.; Meerholz, K.; Würthner, F. *Angew. Chem., Int. Ed.* **2009**, *48*, 8776–8779.
- (19) Bagnis, D.; Beverina, L.; Huang, H.; Silvestri, F.; Yao, Y.; Yan, H.; Pagani, G. A.; Marks, T. J.; Facchetti, A. *J. Am. Chem. Soc.* **2010**, *132*, 4074–4075.
- (20) Yang, D.; Yang, L.; Huang, Y.; Jiao, Y.; Igarashi, T.; Chen, Y.; Lu, Z.; Pu, X.; Sasabe, H.; Kido, J. *ACS Appl. Mater. Interfaces* **2015**, *7*, 13675–13684.
- (21) Jradi, F. M.; Kang, X.; O'Neil, D.; Pajares, G.; Getmanenko, Y. A.; Szymanski, P.; Parker, T. C.; El-Sayed, M. A.; Marder, S. R. *Chem. Mater.* **2015**, *27*, 2480–2487.
- (22) Park, J.; Barbero, N.; Yoon, J.; Dell'Orto, E.; Galliano, S.; Borrelli, R.; Yum, J.-H.; Di Censo, D.; Grätzel, M.; Nazeeruddin, M. K.; Barolo, C.; Viscardi, G. *Phys. Chem. Chem. Phys.* **2014**, *16*, 24173–24177.

- (23) Ehrenreich, P.; Pfadler, T.; Paquin, F.; Dion-Bertrand, L.-I.; Paré-Labrosse, O.; Silva, C.; Weickert, J.; Schmidt-Mende, L. *Phys. Rev. B: Condens. Matter Mater. Phys.* **2015**, *91*, 035304.
- (24) Osedach, T. P.; Andrew, T. L.; Bulović, V. *Energy Environ. Sci.* **2013**, *6*, 711–718.
- (25) Chen, G.; Yokoyama, D.; Sasabe, H.; Hong, Z.; Yang, Y.; Kido, J. *Appl. Phys. Lett.* **2012**, *101*, 083904.
- (26) Ryan, J. W.; Kirchartz, T.; Viterisi, A.; Nelson, J.; Palomares, E. J. *Phys. Chem. C* **2013**, *117*, 19866–19874.
- (27) Cambarau, W.; Viterisi, A.; Ryan, J. W.; Palomares, E. *Chem. Commun.* **2014**, *50*, 5349–5351.
- (28) Wei, G.; Wang, S.; Renshaw, K.; Thompson, M. E.; Forrest, S. R. *ACS Nano* **2010**, *4*, 1927–1934.
- (29) Liu, Y.; Zhang, F.; Dai, H.; Tang, W.; Wang, Z.; Wang, J.; Tang, A.; Peng, H.; Xu, Z.; Wang, Y. *Sol. Energy Mater. Sol. Cells* **2013**, *118*, 135–140.
- (30) Huang, J.-S.; Goh, T.; Li, X.; Sfeir, M. Y.; Bielinski, E. A.; Tomasulo, S.; Lee, M. L.; Hazari, N.; Taylor, A. D. *Nat. Photonics* **2013**, *7*, 479–485.
- (31) Wang, H.; Zheng, Y.; Zhang, L.; Yu, J. *Sol. Energy Mater. Sol. Cells* **2014**, *128*, 215–220.
- (32) Guan, Z.; Yu, J.; Huang, J.; Zhang, L. *Sol. Energy Mater. Sol. Cells* **2013**, *109*, 262–269.
- (33) Gambino, S.; Mazzeo, M.; Genco, A.; Di Stefano, O.; Savasta, S.; Patanè, S.; Ballarini, D.; Mangione, F.; Lerario, G.; Sanvitto, D.; Gigli, G. *ACS Photonics* **2014**, *1*, 1042–1048.
- (34) Cacciola, A.; Di Stefano, O.; Stassi, R.; Saija, R.; Savasta, S. *ACS Nano* **2014**, *8*, 11483–11492.
- (35) Bernstein, J.; Davey, R. J.; Henck, J.-O. *Angew. Chem., Int. Ed.* **1999**, *38*, 3440–3461.
- (36) Cruz-Cabeza, A. J.; Reutzel-Edens, S. M.; Bernstein, J. *Chem. Soc. Rev.* **2015**, *44*, 8619–8635.
- (37) Jones, A. O.; Chattopadhyay, B.; Geerts, Y. H.; Resel, R. *Adv. Funct. Mater.* **2016**, *26*, 2233–2255.
- (38) Balzer, F.; Röthel, C.; Rubahn, H.-G.; Lützen, A.; Parisi, J.; Resel, R.; Schiek, M. *J. Phys. Chem. C* **2016**, *120*, 7653–7661.
- (39) Balzer, F.; Resel, R.; Lützen, A.; Schiek, M. *J. Chem. Phys.* **2017**, *146*, 134704.
- (40) Deing, K. C.; Mayerhöffer, U.; Würthner, F.; Meerholz, K. *Phys. Chem. Chem. Phys.* **2012**, *14*, 8328–8334.
- (41) Gsänger, M.; Kirchner, E.; Stolte, M.; Burschka, C.; Stepanenko, V.; Pflaum, J.; Würthner, F. *J. Am. Chem. Soc.* **2014**, *136*, 2351–2362.
- (42) Qaddoura, M. A.; Belfield, K. D.; Tongwa, P.; DeSanto, J. E.; Timofeeva, T. V.; Heiney, P. A. *Supramol. Chem.* **2011**, *23*, 731–742.
- (43) Liess, A.; Lv, A.; Arjona-Esteban, A.; Bialas, D.; Krause, A.-M.; Stepanenko, V.; Stolte, M.; Würthner, F. *Nano Lett.* **2017**, *17*, 1719–1726.
- (44) Kasha, M.; Rawls, H.; El-Bayoumi, M. *Pure Appl. Chem.* **1965**, *11*, 371–392.
- (45) Davydov, A. S. *Phys. Usp.* **1964**, *7*, 145–178.
- (46) Bialas, D.; Zitzler-Kunkel, A.; Kirchner, E.; Schmidt, D.; Würthner, F. *Nat. Commun.* **2016**, *7*, 12949.
- (47) Spano, F. C.; Silva, C. *Annu. Rev. Phys. Chem.* **2014**, *65*, 477–500.
- (48) von Berlepsch, H.; Möller, S.; Dähne, L. *J. Phys. Chem. B* **2001**, *105*, 5689–5699.
- (49) Meyenburg, I.; Breuer, T.; Karthäuser, A.; Chatterjee, S.; Witte, G.; Heimbrot, W. *Phys. Chem. Chem. Phys.* **2016**, *18*, 3825–3831.
- (50) Austin, A.; Hestand, N. J.; McKendry, I. G.; Zhong, C.; Zhu, X.; Zdilla, M. J.; Spano, F. C.; Szarko, J. M. *J. Phys. Chem. Lett.* **2017**, *8*, 1118–1123.
- (51) Hoffmann, M.; Schmidt, K.; Fritz, T.; Hasche, T.; Agranovich, V.; Leo, K. *Chem. Phys.* **2000**, *258*, 73–96.
- (52) Hestand, N. J.; Spano, F. C. *Acc. Chem. Res.* **2017**, *50*, 341–350.
- (53) Petelenz, P. *Phys. Status Solidi B* **1977**, *83*, 169–175.
- (54) Hestand, N. J.; Spano, F. C. *J. Chem. Phys.* **2015**, *143*, 244707.
- (55) Bardeen, C. J. *Annu. Rev. Phys. Chem.* **2014**, *65*, 127–148.
- (56) Yamagata, H.; Pochas, C. M.; Spano, F. C. *J. Phys. Chem. B* **2012**, *116*, 14494–14503.
- (57) Yamagata, H.; Maxwell, D. S.; Fan, J.; Kittilstved, K. R.; Briseno, A. L.; Barnes, M. D.; Spano, F. C. *J. Phys. Chem. C* **2014**, *118*, 28842–28854.
- (58) Bardeen, C. J. *MRS Bull.* **2013**, *38*, 65–71.
- (59) Hestand, N. J.; Zheng, C.; Penmetcha, A. R.; Cona, B.; Cody, J. A.; Spano, F. C.; Collison, C. J. *J. Phys. Chem. C* **2015**, *119*, 18964–18974.
- (60) Zheng, C.; Penmetcha, A. R.; Cona, B.; Spencer, S. D.; Zhu, B.; Heaphy, P.; Cody, J. A.; Collison, C. J. *Langmuir* **2015**, *31*, 7717–7726.
- (61) Zheng, C.; Bleier, D.; Jalan, I.; Pristash, S.; Penmetcha, A. R.; Hestand, N. J.; Spano, F. C.; Pierce, M. S.; Cody, J. A.; Collison, C. J. *Sol. Energy Mater. Sol. Cells* **2016**, *157*, 366–376.
- (62) Abdullaeva, O. S.; Schulz, M.; Balzer, F.; Parisi, J.; Lützen, A.; Dedek, K.; Schiek, M. *Langmuir* **2016**, *32*, 8533–8542.
- (63) Sheldrick, G. M. *Acta Crystallogr., Sect. A: Found. Adv.* **2015**, *71*, 3–8.
- (64) Sheldrick, G. M. *Acta Crystallogr., Sect. C: Struct. Chem.* **2015**, *71*, 3–8.
- (65) Macrae, C. F.; Bruno, I. J.; Chisholm, J. A.; Edgington, P. R.; McCabe, P.; Pidcock, E.; Rodriguez-Monge, L.; Taylor, R.; van de Streek, J.; Wood, P. A. *J. Appl. Crystallogr.* **2008**, *41*, 466–470.
- (66) Thévenaz, P.; Rüttimann, U.; Unser, M. *IEEE T. Image. Process.* **1998**, *7*, 27–41.
- (67) Balzer, F.; Sun, R.; Parisi, J.; Rubahn, H.-G.; Lützen, A.; Schiek, M. *Thin Solid Films* **2015**, *597*, 104–111.
- (68) Balzer, F.; Schiek, M. In *Bottom-Up Self-Organization in Supramolecular Soft Matter*; Müller, S. C.; Parisi, J., Eds.; Springer Series in Materials Science; Springer: Berlin, 2015; Vol. 217; Chapter 7, pp 151–176.
- (69) Schneider, C. A.; Rasband, W. S.; Eliceiri, K. W. *Nat. Methods* **2012**, *9*, 671–6675.
- (70) Wang, S.; Hall, L.; Diev, V. V.; Haiges, R.; Wei, G.; Xiao, X.; Djurovich, P. I.; Forrest, S. R.; Thompson, M. E. *Chem. Mater.* **2011**, *23*, 4789–4798.
- (71) Chen, G.; Sasabe, H.; Sasaki, Y.; Katagiri, H.; Wang, X.-F.; Sano, T.; Hong, Z.; Yang, Y.; Kido, J. *Chem. Mater.* **2014**, *26*, 1356–1364.
- (72) Viterisi, A.; Montcada, N. F.; Kumar, C. V.; Gispert-Guirado, F.; Martin, E.; Escudero, E.; Palomares, E. *J. Mater. Chem. A* **2014**, *2*, 3536–3542.
- (73) Mayerhöffer, U.; Gsänger, M.; Stolte, M.; Fimmel, B.; Würthner, F. *Chem. - Eur. J.* **2013**, *19*, 218–232.
- (74) Lambert, C.; Koch, F.; Völker, S. F.; Schmiedel, A.; Holzapfel, M.; Humeniuk, A.; Röhr, M. I.; Mitric, R.; Brixner, T. *J. Am. Chem. Soc.* **2015**, *137*, 7851–7861.
- (75) Kaczmarek-Kedziera, A.; Kedziera, D. *Theor. Chem. Acc.* **2016**, *135*, 214.
- (76) Martínez Martínez, V.; López Arbeloa, F.; Bañuelos Prieto, J.; Arbeloa López, T.; López Arbeloa, I. *J. Phys. Chem. B* **2004**, *108*, 20030–20037.
- (77) Martínez Martínez, V.; López Arbeloa, F.; Bañuelos Prieto, J.; López Arbeloa, I. *J. Phys. Chem. B* **2005**, *109*, 7443–7450.
- (78) Spano, F. C. *Acc. Chem. Res.* **2010**, *43*, 429–439.
- (79) Kistler, K.; Pochas, C.; Yamagata, H.; Matsika, S.; Spano, F. *J. Phys. Chem. B* **2012**, *116*, 77–86.
- (80) Parsons, S. *Acta Crystallogr., Sect. D: Biol. Crystallogr.* **2003**, *59*, 1995–2003.
- (81) Bando, K.; Nakamura, T.; Fujiwara, S.; Masumoto, Y.; Sasaki, F.; Kobayashi, S.; Shimoi, Y.; Hotta, S. *Phys. Rev. B: Condens. Matter Mater. Phys.* **2008**, *77*, 045205.
- (82) Hestand, N. J.; Yamagata, H.; Xu, B.; Sun, D.; Zhong, Y.; Harutyunyan, A. R.; Chen, G.; Dai, H.-L.; Rao, Y.; Spano, F. C. *J. Phys. Chem. C* **2015**, *119*, 22137–22147.
- (83) Bloss, F. D. *An Introduction to the Methods of Optical Crystallography*; Holt Rinehart and Winston, 1961.
- (84) Nesse, W. *Introduction to Optical Mineralogy*, 3rd ed.; Oxford University Press: New York, 2004.
- (85) Craig, J.; Vaughan, D. *Ore Microscopy and Ore Petrology*; John Wiley & Sons: New York, 1981.
- (86) Viney, C. *Polym. Eng. Sci.* **1986**, *26*, 1021–1032.